A grid connected photovoltaic system using a parallel multilevel inverter: Optimal number of inverter cells

Chabakata MAHAMAT *[1, 2] and El hassane Margoum[3]
[1]Univeristé d'Angers - IUT d'Angers-Cholet, département GEII, Laboratoire LARIS
[2] Université de Guyane, DFR- ST, Laboratoire UMR ESPACE-DEV(228)
[3]Department of electrical engineering, National school of applied science, Ibn-Tofail University, Kenitra, Morocco
emails: chabakata.mahamat@univ-angers.fr;chabakata.mahamat@univ-guyane.fr
elhassane.margoum@uit.ac.ma

Abstract – This paper presents a grid connected photovoltaic (PV) system using a parallel multicellular inverter (PMI). We focus on the optimized design of an LCL filter connecting a parallel multicellular inverter by looking for the number which optimizes the losses of the inverter, as well as the energy management by controlling the power produced by the photovoltaic generator (PVG). In order to transfer the power produced by the PVG to the grid, the classical maximum power point tracking ($MPPT$) algorithm called perturb and observe ($P\ \&\ O$) is used to maximize the power produced by the PVG. The active and reactive power control (PQ control) using a Phase-Locked Loop (PLL) for synchronization is applied to the inverter. We present the value of this innovative PV architecture using a PMI compared to the conventional one. We show that this PQ control, although it is classical, is well adapted to the PV architecture using a PMI. We also present and discuss the simulation results obtained by using the Matlab software (simulink and simpowersystems).

Keywords — Grid-connected PV system; optimal LCL filter design; PQ control; PLL; Parallel Multicellular Inverter

1. INTRODUCTION

In grid-connected photovoltaic (PV) systems. static converters plays an essential role in converting and preserving the quality of electrical energy. Indeed, maximizing the power transfer from the Photovoltaic Generator (PVG) to the electrical grid and optimizing the system dynamics both depend on the static converter technology used and its control algorithms [1], [2], [3], [4]. In conventional PV system, a LCL filter is often used to connect the inverter to the utility grid in order to obtain a good attenuation of high frequency harmonics generated by the inverter [5], [6], [7], [8], [9]. However, even with an LCL filter, the passive components of the filter remain bulky, heavy and expensive. Especially if it must meet the requirements of the $IEEE1547$electrical interconnection standard [10]. In addition. the control of the conventional PV system requires a sophisticated control method (sliding mode, control by return of states, cascading etc.) because it is a third order filter (the capacitive effect is not negligible) [11], [12], [13], [14], [15].

Hence the importance of using a parallel multicellular inverter (PMI) whose waveform is better quality and easily filterable with small passive components of the filter. Especially, from a control point of view, the capacitive effect can be neglected here and the filter order is reduced from third order to first order as in [16]. But the use of this PMI converter requires the search for the optimal number of cells of the inverter that optimizes the system. That is to say which gives a better compromise between the quality of the energy, and the volume. Therefore the use of this innovative PV architecture using a PMI in this domain should allow a gain in volume of the filter, in system reliability and in quality of energy. We deal with these issues in this paper.

So the objective of this work is to analyze the PV system with PMI converter and to show that this is a very interesting structure compared to the conventional solution. We are particularly interested in control and sizing of this system, in a context of use where, the system efficiency and the reliability issues of the system should be taken into account. The grid considered is low voltage with a RMS voltage equal to 230 V and a frequency equal to 50 Hz but may vary in which a power of a few kilowatts (kW), depending on the number of PV panel is injected.

This work is organized around the following sections: section *2* describes the system under study, section *3* presents the modeling of the system, section *4* presents the control of the system. Finally, section *5* presents the simulation results and discussions.

2. DESCRIPTION OF THE SYSTEM

Figure 1 shows the proposed architecture of the grid connected PV system.

The system is composed of the PVG, the three-phase PMI, the LCL filter and the utility grid. It is controlled by a conventional decoupled active and reactive control (PQ control) combined with a conventional Maximum Power Point Tracking Perturb and Observe ($MPPT$ P&O).

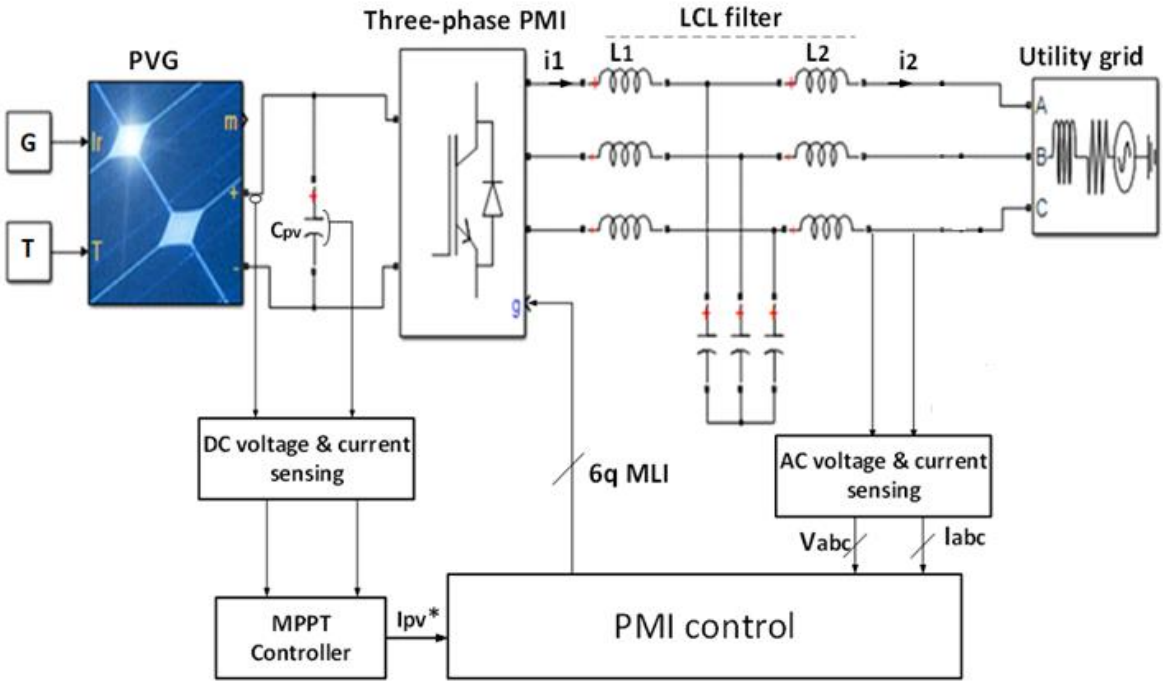

Figure 1 Diagram of the grid-connected **PV** system and its control

3. MODELING AND SIZING OF THE SYSTEM

3.1.4. modeling of the Photovoltaic generator (PVG)

The PVG was modeled according to irradiance G and temperature T. Under standard conditions of temperature and irradiance ($= 25\,\mathrm{C}^\circ$ and $G = 1000\,\mathrm{W/m^2}$) as shown in Figure 1. This *PVG* is composed of forty (40) "SolarWord SW260 mono" *PV* panels [17] connected in series and in parallel to provide a power of ten kilowatts (10 kW).

Thus, the basic element of the *PVG* is a *PV* cell which is a pn - junction of silicon whose behavior is comparable to a current source in parallel with a diode.

In the ideal case, a *PV* cell can be modeled by a current generator in parallel with a diode. In this configuration the current injected by the source is representative of the irradiance and *PV* cell surface.

In the real case, a finer model adds two resistances (Cf. Figure 2). One in series (R_s) and the other in parallel (R_{sh}). R_s characterizes the voltage drops due to the connection contacts between the different cells while R_{sh}characterizes the leakage current in the diode [1], [3]. A double-diode *PV* cell models exist in the literature as in [18] and in [19]. A comparative study between single-diode and double-diode model of *PV* cell was made in [19].To simplify, we choose the single-diode *PV* cell. In this case, the equivalent electrical model of a *PV* cell is given in Figure 2.

Where:

I_{ph} : Photocurrent (in A)

I_{pv} : Cell current (in A)

V_{pv} : Cell voltage (in V)

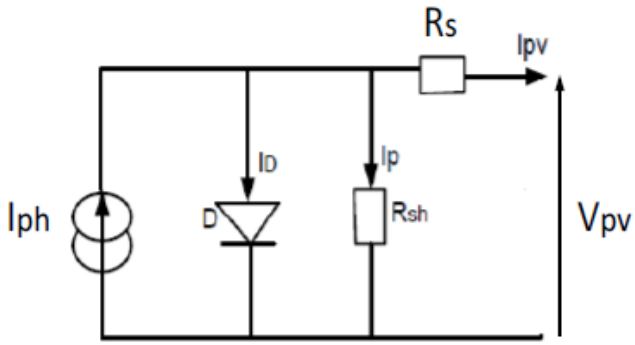

Figure 2. Equivalent diagram of a **PV** cell **[1]**

Mathematical model that governs the scheme of Figure 2 is indicated in (1).

$$I_{pv} = I_{ph} - I_s\left[e^{\frac{Q(V_{pv}+R_s\cdot I_{pv})}{n\cdot K\cdot T}} - 1\right] - \frac{V_{pv}+R_s\cdot I_{pv}}{R_{sh}} \quad (1)$$

I_s : Saturation current of the diode (in A)

T : Cell temperature (in K)

n : Quality factor of the cell (n is between 1 and 2)

K : Boltzmann constant. K = 1.38 10^{-23}(in J/K)

Q : Charge of an electron. Q = 1.16.10^{-19} (in C)

3.2.4. Principle of the Multicellular Parallel Inverter

The simplified diagram of the three-phase *PMI* with q interleaved magnetically independent cells is shown in Figure 3. The *PVG* is replaced here by its *DC* voltage (V_{pv}).

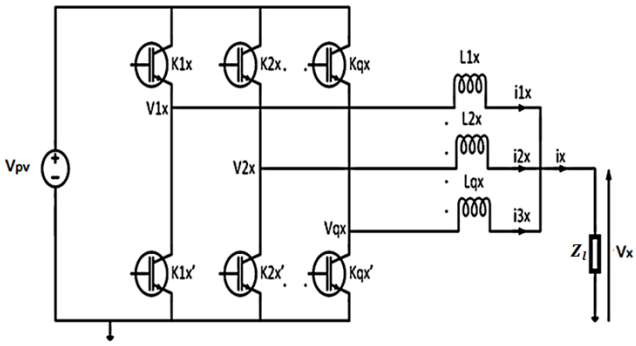

Figure 3. Three-phase **PMI** with $\boldsymbol{q}$ interleaved cells [20]

Where: $x = a, b, c$ is the name of the considered phase of the inverter. q is the number of the interleaved cells. L_{ix} $(i = 1,2, \dots q)$ are the cell interleaving inductances (inverter side inductances). $K_{ix}$and K'_{ix} are the switches of the inverter.

Three-phase PMI interleaved cells have already been studied in [1], [16], [20], [21] and [22]. This converter is also available as a $DC\ /\ DC$ boost converter [23], [24].

As in a conventional inverter, the two switches of the same inverter arm are controlled complementarily.

$K_{ix} = \overline{K'_{ix}}$; where $i = \{1, 2. \dots . . q\}$ and $x = \{a, b, c\}$.

The q different switching cells are shifted by $\frac{2\pi}{q}$ and controlled with the same duty cycle [3], [4]. The three phases of the inverter (a, b, c) are also shifted by $\frac{2\pi}{3}$.

To simplify, the study of the three-phase inverter can be reduced to a single phase. Figure 4 shows the waveforms of a one phase of the $PMI$with four independent interleaved cells when a RL load is connected [20].

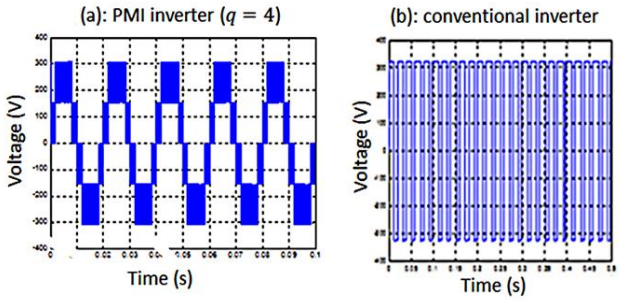

Figure 4. Waveforms of the **PMI** voltage vs time [20]

It can be seen that contrary to the waveform of the conventional inverter (Figure 4.b), the waveform of the PMI is more sinusoidal (Figure 4.a). Indeed, the harmonic content of this waveform is less rich in harmonics. Moreover, these harmonics are at the apparent frequency which is equal to q times the switching frequency. So it is easy to filter them. We can therefore use small caliber passive elements (less bulky and less expensive) to make the filter. In addition, dividing the output power makes it possible to choose small caliber switches (less expensive) thus reducing the overall volume and cost of the system.

3.2.1. Equation of tensions: temporal approach

In order to comply with the $IEEE1547$ standard for interconnection of electrical systems [10], capacitors and inductances have been added to the cell interleaving inductances of the PMI thus forming an LCL filter, R_f resistances has also been added to dampen the resonance phenomenon caused by capacitors. The load Z_l (see Figure 3) is also replaced by the utility grid which is modeled by a voltage source (V_{gx}) in series with an inductance (included in L_{2x}). Where L_{2x} are the grid side inductances. To facilitate modeling, a fictitious neutral marked 0 was created. In this case, Figure 5 shows the grid connected PMI.

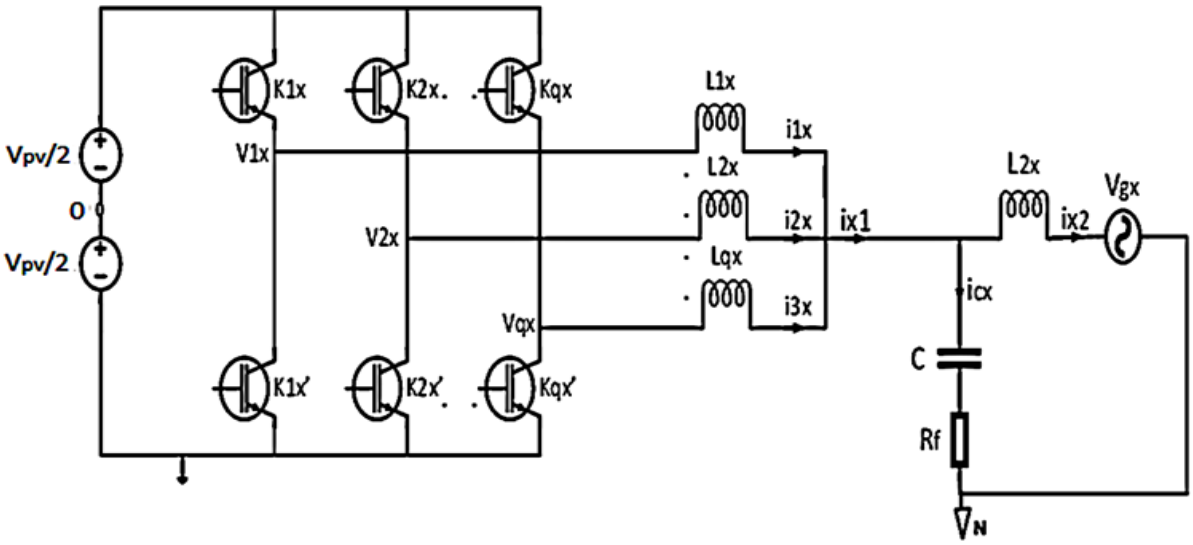

Figure 5. Simplified grid connected **PMI**

The inverter voltages relative to the fictitious neutral noted (V_{ix0}) take discrete values as shown in (2).

Where $i = 1,2,..q$ and $x = a,b,c$.

$$\begin{cases} V_{ix0} = \frac{V_{pv}}{2} \;\; if \; K_{ix} = 1 \;\; and \; K_{ix}{}' = 0 \\ V_{ix0} = -\frac{V_{pv}}{2} \;\; if \; K_{ix} = 0 \; and \;\; K_{ix}{}' = 1 \end{cases} \quad (2)$$

By applying the law of meshes in Figure 5, we obtain (6).

$$V_{ix0} - V_{ixn} - V_{n0} = 0 \quad (3)$$

Where V_{n0} is the common mode voltage and $V_{ixn}$are the line to neutral inverter voltages.

By developing equation (3) the following equation systems are obtained for the three phases of the interleaved cell inverter:

$$\begin{cases} V_{1a0} - V_{1an} - V_{n0} = 0 \\ V_{2a0} - V_{2an} - V_{n0} = 0 \\ \quad . \\ V_{qa0} - V_{qan} - V_{n0} = 0 \\ V_{1b0} - V_{1bn} - V_{n0} = 0 \\ V_{2b0} - V_{2bn} - V_{n0} = 0 \\ \quad . \\ V_{qb0} - V_{qbn} - V_{n0} = 0 \\ V_{1c0} - V_{1cn} - V_{n0} = 0 \\ V_{2c0} - V_{2cn} - V_{n0} = 0 \\ \quad . \\ V_{qc0} - V_{qcn} - V_{n0} = 0 \end{cases} \quad (4)$$

Summing up the elements of (4) and assuming that the set of simple voltages forms a balanced system of $3q$ phases, the second column of (4) disappears. So (4) becomes (5).

$$\sum_{x=a}^{c} \sum_{i=1}^{q} V_{ix0} - 3qV_{n0} = 0 \quad (5)$$

Therefore, the common mode voltage is expressed by (6).

$$V_{n0} = \frac{\sum_{x=a}^{c} \sum_{i=1}^{q} V_{ix0}}{3q} \quad (6)$$

Knowing the common mode voltage V_{n0}, and the cell voltage vector of the inverter V_{ix0} (relative to the fictitious neutral) and by using (3), we can deduce the expression of the line to phase voltage vector of the inverter in (7).

$$V_{ixn} = V_{ix0} - V_{n0} \quad (7)$$

From these equations, we now focus on the design of the passive elements of the LCL filter.

3.2.2. Electrical sizing of passive elements

Passive electrical sizing consists in determining the values of passive elements of the Figure 5 by respecting the standard $IEEE1547$ which imposes a voltage drop and a current ripple to be respected [10].

To simplify the study, from Figure 5 we set:

$V_{ixn} = V_1$, $L_{1x} = L_{2x} = L_{3x} \ldots = L_{qx} = L_1$,

$i_{x1} = i_1$, $i_{x2} = i_2$, $i_{cx} = i_c$, $L_{2x} = L_2$ and $V_g = V_2$.

In this case, Figure 5 becomes Figure 6.

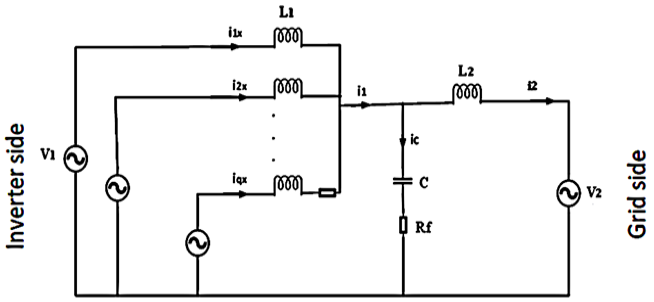

Figure 6. Simplified diagram of the LCL filter

The challenge is now what are the minimum values of the passive elements of the LCL filter to comply with the $IEEE1547$ standard ?

This $IEEE1547$ standard allows [10]:

- Inverter side current ripple: $10\% \cdot i_1 \leq \Delta i_1 \leq 20\% \cdot i_1$
- Grid side current ripple equal to $\Delta i_2 = 0.3\% \cdot i_2$
- Drop voltage equal to $\Delta V_L = 10\% \cdot V_2$
- Variation of reactive power equal to $Q_c \leq 5\% \cdot P_n$.

Where: P_n is the rated power, $i_1 = \frac{P_n}{3V_1}$ is the inverter side current and $i_2 = \frac{P_n}{3V_2}$ is the grid side current.

Indeed, $S_n = P_n + Q_n$. But we don't inject reactive power into the grid. So thanks to the PQ control, we must be able to set the reactive power to zero ($Q_n = 0$). So the apparent power is equal to the active power ($S_n = P_n$).

To calculate the values of passive elements of the LCL filter, many authors impose simplifying hypotheses in which they connect the neutral of the utility grid to the midpoint of the inverter (fictitious neutral: point 0) and consider the inverter as a DC converter to find the current ripple expression as a function of inductance, switching frequency, DC voltage (V_{pv}) and duty cycle [25]. Knowing the ripple formula allows to find the inductance on the inverter side. The value of the capacitor is found by using the formula of the reactive power generated by the capacitor. Then, knowing L_1 and C and by using the transfer function of the LCL filter, it is easy to find the grid side inductance L_2.

But their method is based on unrealistic assumptions. Indeed, in the case of the inverter, the duty cycle changes over time. The output voltage of the inverter is also a function of time and depends on the grid voltage [25].

In [1] and [25], authors calculated the value of passive elements by numerical method which consists in calculating the Fast Fourier Transform (FFT) of currents and voltages on both sides of the LCL filter. This method gave us the elements of Table 1.

Table 1. Electrical parameters of the system

Symbol	Parameter	Value	Unit
P_n	Rated power	10	kW
V_{pv}	PV voltage	700	V
V_2	Grid RMS grid voltage	230	V
f_{sw}	Switching frequency	20	kHz
f	Grid frequency	50	Hz
ΔI_{1m}	Maximum inverter side current ripple	$20\% \cdot i_1 \approx 3$	A
ΔI_{2m}	Maximum grid side current ripple	$0.3\% \cdot i_2 \approx 43.5$	mA
L_1	Inverter side inductance	3.5	mH
L_2	Grid side inductance	3	mH
R_1	Inverter side resistance	0.5	Ω
R_2	Grid side resistance	0.5	Ω
C	Capacity	1.5	µF
R_f	Damping resistance	3.86	Ω

Knowing the electrical values of the system parameters, we now focus on the physical dimensioning of the filter inductances.

3.2.3. Physical design of inductances L_1 and L_2

Knowing the values of $L_1$and L_2 (see Table 1) we are interested in their physical design which consists of determining the magnetic core, the number of turns, the air gap value, the joule losses, the iron losses and the temperature rise of each inductance. For this, we have based on the area product method presented in [25] and [26]. Knowing the rated current flowing through each inductance, it is possible to reasonably choose a current density and thus to calculate the section of the conductor that is necessary to carry out the winding of the inductance. As indicated in Figure 7, the method is summarized here in eight steps (where $k = 1,2$).

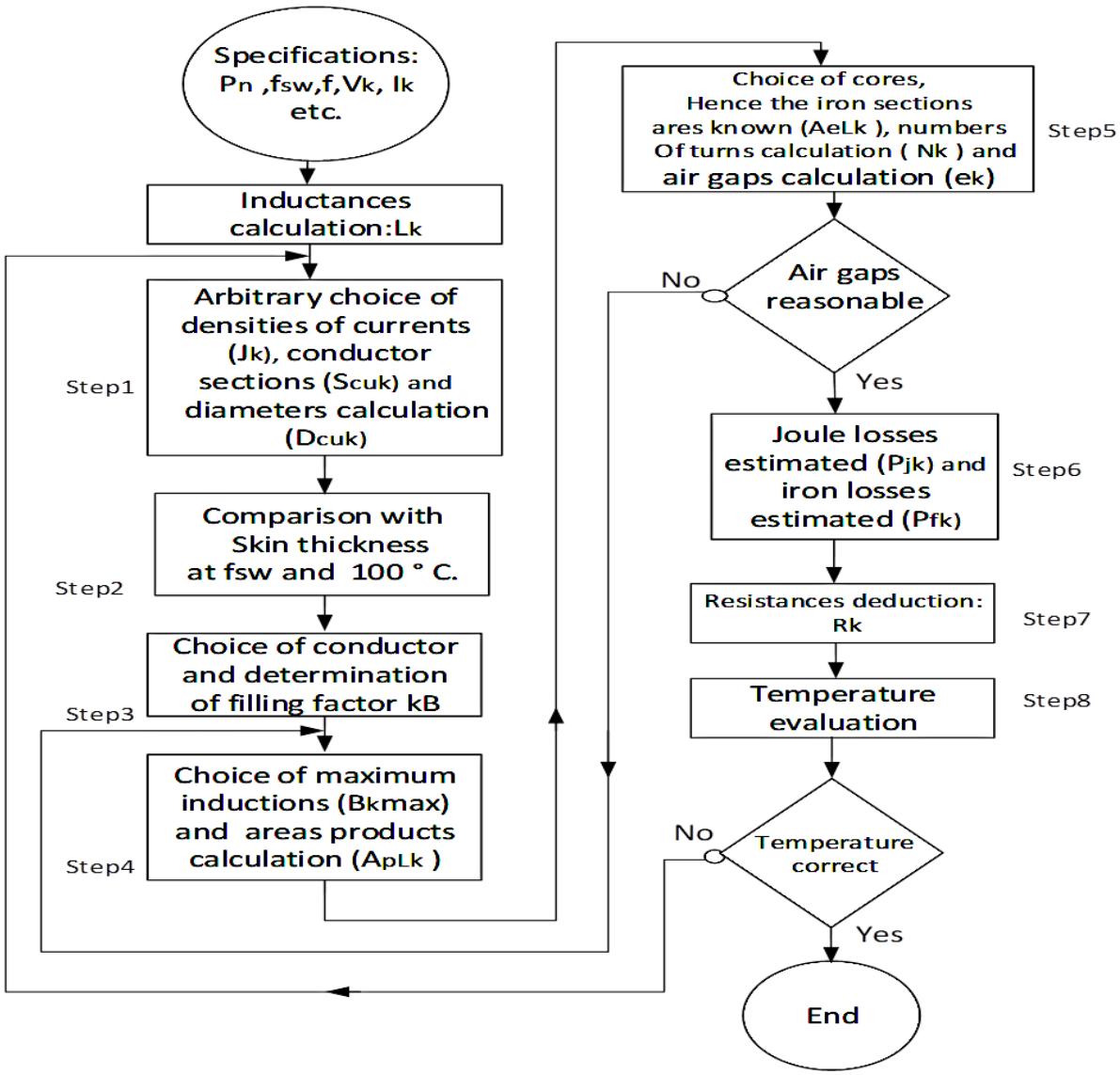

Figure 7. Principle of the area product metho

3.2.3.1. Classical steps of the method (from step 1 to step 5)

In this section, we group all the classical steps of the method, that is from step 1 to step 5.

Knowing the effective current, the first step consists of choosing the density of the current (J_k) in order to calculate the diameter and section of the copper. In general, J_k is between 1 A / mm^{2}and 10 A / mm^2 [26]. The formula for the copper section is given in (8). Where $k = 1,2$ ($k = 1$ indcates the inverter side element whereas $k = 2$, indicates the grid side element).

$$S_{cuk} = \frac{I_k}{J_k} \tag{8}$$

Where: S_{cuk}, copper section of the conductor; I_k, effective current; J_k, current density.

From (8), we can deduce the formula of the copper diameter in (9). Where D_{cuk} ($k = 1,2$) is the cooper diameter of the conductor.

$$D_{cuk} = \sqrt{\frac{4 \cdot S_{cuk}}{\pi}} \tag{9}$$

This diameter of the conductor is compared to the skin thickness at the temperature equal to $100\ ^\circ C$. Equations (10) and (11) indicate the skin thickness at T_0 and T_1, respectively. Where T_0 and T_1 are the considered temperatures ($T_0 = 20$ °C and $T_1 = 100$ °C).

$$\delta_0 = \frac{1}{\sqrt{\sigma_0 \cdot \mu \cdot \pi \cdot f_{sw}}} \tag{10}$$

$$\delta_1 = \frac{1}{\sqrt{\rho_0 [1+\alpha(T_1 - T_0)] \cdot \mu \cdot \pi \cdot f_{sw}}} \tag{11}$$

Where:$\rho_0 = 0.0172\ \mu\Omega \cdot \mathrm{m}$, copper resistivity at T_0; σ_0, copper conductivity ($\sigma_0 = \frac{1}{\boldsymbol{\rho_0}} = 58.1\ \mu\Omega^{-1} \cdot \mathrm{m}^{-1}$), δ_1, skin thickness at T_1; δ_0, skin thickness at T_0; α, copper coefficient ($\alpha = 0.0038$); μ, permeability of the medium; μ_0, Vacuum permeability; μ_r, relative permeability. $\mu = \mu_0 \cdot \mu_r = \mu_0 = 4\pi \cdot 10^{-7}$ H/m (because copper permeability is equal to $\mu_r = 1$ H/m).

Table 2 summarizes the evolution of the skin thickness according to the cutting frequency.

Table 2. Evolution of the skin thickness

Frequency	5 kHz	10 kHz	20 kHz	25 kHz	50 kHz
skin thickness at 20°C (δ_0)	930 µm	660µm	467µm	417µm	295µm
skin thickness at 100°C (δ_1)	1100 µm	754µm	533µm	477µm	337µm

The choice of the conductor is made by comparing the diameter of the conductor's copper to the skin thickness at $T_1 = 100$ °C and according to the switching frequency of the system. In our case, the switching frequency is fixed to $f_{sw} = 20$ kHz so $\delta_1 = 533$ µm.

The choice of the conductor allow to calculate the filling coefficient (k_B) and the expansion factor (k_F). Where k_B is the filling coefficient and k_F is the expansion factor. k_B is the ratio between the wire section (copper + insulator) and the copper section ($k_B = \frac{wire\ section}{copper\ section}$) whereas k_F takes into account the difference between the circular shape of the conductor and the rectangular shape of the wire insulation. For a circular cable, $k_F = \frac{circle\ surface}{square\ surface} = \frac{\pi r^2}{a^2} = \frac{\frac{\pi \cdot a^2}{4}}{a^2} = \frac{\pi}{4}$.

In general, one adopts a value of coefficient of expansion $k_F = 0.5$.

To calculate the areas product, it is necessary to calculate the winding surface (S_{bk}) and the iron section (A_{ek}). They are given in (12) and (13) respectively [1], [26].

$$A_{ek} = \frac{L_k \cdot I_{kmax}}{N_k \cdot B_{max}} \tag{12}$$

$$S_{bk} = N_k \cdot S_{cuk} \cdot \frac{k_B}{k_F} = N_k \cdot \frac{I_{ke}}{k_F \cdot J_k} \cdot k_B \tag{13}$$

Where: L_k, inductance ($k = 1,2$); I_{kmax}, maximum current; B_{max}, maximum induction [27] (generally, $B_{max} = 300$ mT for ferrite cores); N_k, number of turns.

Hence the areas product (A_{pLk}):

$$A_{pLk} = A_{ek} \cdot S_{bk} = k_B \cdot \frac{L_k \cdot {I_{kmax}}^2}{\sqrt{2} \cdot k_F \cdot J_k \cdot B_{max}} \tag{14}$$

Once the areas product is calculated, a magnetic core must be chosen whose areas product is greater than or equal to the calculated areas product by using (14) [26].

For example, if the calculated areas product is equal to $A_{pLk} = 314800$ mm^4, we can choice magnetic core whose areas product is equal to $A_{pn} = 349180$ mm^4 [27].

The knowledge of the iron section allow to calculate the number of turns as shown in (15).

$$N_k = \frac{L_k \cdot I_{kmax}}{A_{ek} \cdot B_{max}} \tag{15}$$

To calculate the length of gaps we have:

$$L_k = \frac{{N_k}^2}{R_{tot}} \tag{16}$$

Where: R_{tot}, total reluctance; L_k, inductance; and N_k, number of turns. The total reluctance which is the sum of the reluctance of the iron and the air-gap as indicated in (17).

$$R_{tot} = R_{iron} + R_{\mathrm{air-gap}} \tag{17}$$

Iron and air-gap reluctances are indicated in (18) and in (19) respectively.

$$R_{iron} = \frac{l_e}{\mu \cdot \mu_0 \cdot A_{ek}} \tag{18}$$

$$R_{\text{air-gap}} = \frac{e_k}{\mu_0 \cdot A_{ek}} \quad (19)$$

Where: l_e, average length of the field line; e_k, air-gap length.

By replacing R_{iron} and $R_{\text{air-gap}}$ with their expressions, (16) becomes (20).

$$L_k = \frac{{N_k}^2}{\frac{l_e}{\mu \cdot \mu_0 \cdot A_{ek}} + \frac{e_k}{\mu_0 \cdot A_{ek}}} = \frac{{N_k}^2 \cdot \mu_0 \cdot A_{ek}}{\frac{l_e}{\mu} + e_k} \quad (20)$$

Moreover, if we formulate the hypothesis of the concentration of electromagnetic energy in air-gap, the inductance is expressed by (21). Indeed, to calculate the air gap, we can make the approximation according to which electromagnetic energy in the magnetic core is negligible compared to that of the air-gap. That is $\frac{l_e}{\mu_r} \ll e_k$ [26].

$$L_k = \frac{{N_k}^2 \cdot \mu_0 \cdot A_{ek}}{\frac{l_e}{\mu_r} + e_k} \Rightarrow L_k = \frac{{N_k}^2 \cdot \mu_0 \cdot A_{ek}}{e_k} \quad (21)$$

So we can deduce the air-gap length in (22).

$$e_k \approx \frac{{N_k}^2 \cdot \mu_0 \cdot A_{ek}}{L_k} \quad (22)$$

Now, we discuss the losses in the LCL filter in the following section.

3.2.3.2. Estimates LCL filter losses

In this section, we estimate the losses in the LCL filter which are composed of losses in the inductances and losses due to the capacitors and the damping resistances. Losses in the inductances are consisting of joule losses and iron losses.

Iron losses in the inductances are lower in the case of losses due to the small ripple of the current in the inductances. Joule losses can be minimized by varying the length and number of turns.

Joule losses P_{jk} $(k = 1, 2)$ are calculated according to the following formula.

$$P_{jk}(f) = \sum_{i=1}^{h} R_k(f) \cdot I_k(f)^2 \quad (23)$$

Where: f, working frequency; $i = 1, \ldots h$ represents the frequency components; R_k, internal resistances of the inductances and I_k, effective currents ($k = 1, 2$).

For $k = 1$, we obtain the joules losses in inductance L_1 and for $k = 2$, we have the joules losses in L_2.

The formula of the resistance is indicated in (24).

$$R_k(f) = \frac{\rho \cdot N_k \cdot \mathrm{L_n}}{S_e(f)} \quad (24)$$

Where: ρ, material resistivity; N_k, number of turns; L_n, average length of a spire and S_e, effective conductor section (copper + insulator).

To estimate iron losses, we consider the Steinmetz model [26] given in equation (25).

$$P_v = k_{st} \cdot {B_{max}}^{\alpha_{st}} \cdot f^{\beta_{st}} \quad (25)$$

Where: P_v (in kW/m^3) is the density iron losses; B_{kmax} (in mT) is the maximum material induction; f (in kHz) is the working frequency; k_{st}, α_{st} and β_{st} are the coefficients of Steinmetz (without unit). Iron losses are then calculated by multiplying the sum of the density iron losses (P_v) by the volume of the magnetic core (V_{ek}) as in (26).

$$P_{iron\_k} = V_{ek} \cdot \sum_{i=1}^{h} P_v \quad (26)$$

Where: P_{iron_k} iron losses; V_{ek}, magnetic core volume; $i = 1, .. h$ represents the frequency components.

Losses due to capacitor and damping resistance are expressed by (27) [1].

$$P_{C\_R_f} = \sum R_s \cdot I_c(h)^2 + \sum R_f \cdot I_c(h)^2 \quad (27)$$

Where: R_s, capacitor internal resistance; R_f, damping resistance and $I_c(h)$ is the effective current flowing through the capacitor.

Knowing the losses in the inductances, we can now evaluate the temperature in the magnetic circuit. The losses in the capacitor and the damping resistance do not affect the temperature of the magnetic circuit.

3.2.3.3. Evaluation of the circuit temperature

In reality, a thermal model of a magnetic circuit contains a thermal resistance of convection between the core and the ambient, a thermal resistance of conduction between the conductors and the core and a thermal resistance of convection of the conductors. To simplify, we choose the simplified thermal model presented in [1] and indicated in the following equation.

$$R_{th\_k} = \frac{\Delta T}{P_{iron\_k} + P_{jk}} \Rightarrow \Delta T = R_{th\_k} \cdot \left(P_{iron\_k} + P_{jk}\right) \quad (28)$$

Where: R_{th_k}, thermal resistance [27] (given by the manufacturer) and ΔT is the temperature difference ($\Delta T = T_{max} - T_{amb}$; T_{max}, maximum temperature; T_{amb}, ambient temperature).

3.2.3.3. Estimations of losses in the inverter

Losses due to the inverter consist of the conduction losses and switching losses of the inverter switches. The switching and conduction losses of the converter are given by equations (29) and (30) respectively [1].

$$P_{com} = \frac{V_{pv}}{V_{CE}} \left(E_{com} \cdot f_{sw}\right) \quad (29)$$

$$P_{cond} = \frac{V_{pv}}{V_E}\left[V_0 . I_{moy} + R_{on} . {I_k}^2\right] \quad (30)$$

Where: P_{com}, switching losses; P_{cond}, conduction losses; V_{pv}. PV voltage (input DC voltage of the inverter); V_{CE}, the voltage indicated in the transistor datasheet; E_{com}, switching energy; f_{sw}, switching frequency; V_0, threshold voltage of the switch; R_{on}, resistance of the switch; I_k, effective current.

In order to estimate the losses in the inverter, we considered the 1.2 kV /10 A module [28] from "infineon" (referenced by: FS10R12VT3) which meets our specifications in terms of maximum current, DC input inverter voltage and switching frequency [1].

3.2.4. System efficiency calculation

System efficiency is given by (31).

$$\eta = \frac{(P_n - P_{tot})}{P_n} \times 100 \quad (31)$$

Where: P_n, rated power ($P_n = 10$ kW); P_{tot},total system losses.

Table 3 shows losses of the global system (inverter + filter) and system efficiency as a function of the cells number q ($q = 1, \ldots 8$).

Where: $P_j = P_{j1} + P_{j2}$, total joule losses in L_1 and L_2; $P_{iron} = P_{iron\_1} + P_{iron\_2}$, total iron losses;

$P_{tot\_LCL} = P_j + P_{iron} + P_{C\_Rf}$, total LCL filter losses, $P_{tot} = P_{tot\_LCL} + P_{tot\_Sc}$, total system losses; $P_{tot\_Sc} = P_{com} + P_{cond}$, total semiconductors losses;

Table 3. System result

Symbol	Signification	Value								Unity
q	Cell number	1	2	3	4	5	6	7	8	
P_j	Joule losses	878	503.6	503.87	332.7	346.5	491.56	515.23	634.52	W
P_{iron}	Iron losses	65.82	30.4	38.4	35.9	0.04	0.045	0.05	0.057	mW
P_{C_Rf}	Losses in C and R_f	0.96	0.24	0.13	0.098	0.087	0.084	0.08	0.07	W
P_{tot_LCL}	total losses in LCL filter	944.7	503.6	503.87	332.7	346.55	491.62	515.28	634.52	W
P_{cond}	conduction losses	220.74	145.5	144.24	142.92	142.56	142.86	143.2	143.87	W
P_{com}	switching losses	264.16	224.7	187.23	166.93	154.47	146.13	140.1	135.58	W
P_{tot_Sc}	total losses in semiconductors	484.9	370.3	331.47	309.84	297	288.98	283.32	279.46	W
P_{tot}	total system losses	1400	874.12	862.5	642.65	643.67	780.6	798.68	914.06	W
η	System efficiency	86	91.3	91.4	93.6	93.5	92.2	92	90.86	%

Figure 8 shows total losses and system efficiency as a function of the cells number (q).

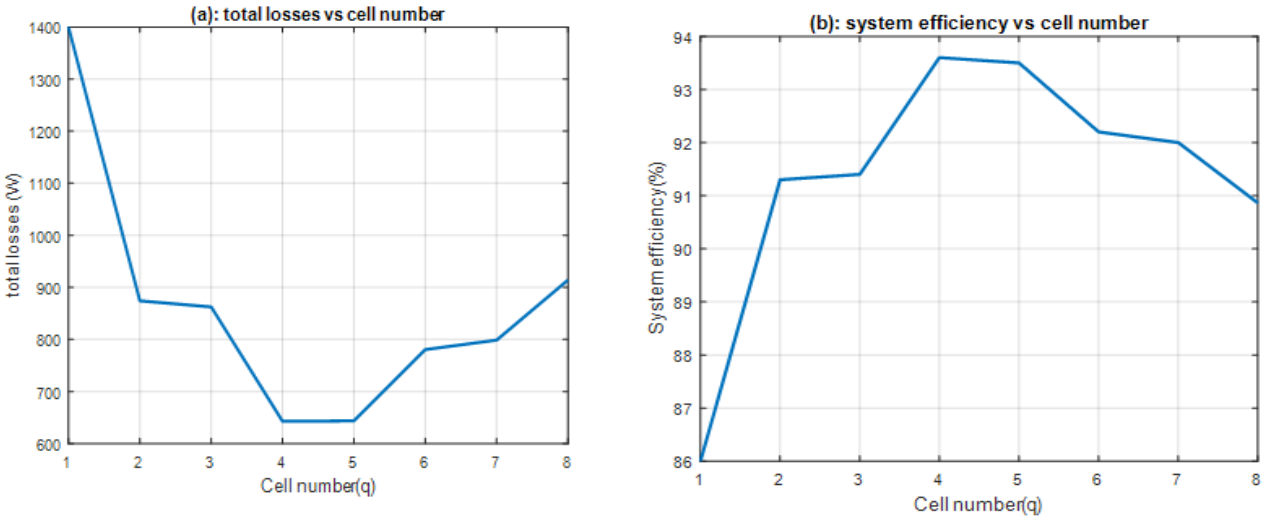

Figure 8. Total losses (a) and system efficiency (b) vs cell number

As shown in Figure 8, optimal cell number which optimizes the losses is obtained for $q = 4$. Indeed, in the case of $q = 4$, total losses are lower ($P_{tot} = 642.65$ W) as shown in Figure 8.a. This gives the highest system efficiency ($\eta = 93.6$ %) as shown in Figure 8.b.

So our optimal number of cell is equal to $q = 4$.

We are now interested in control of the system in the following section.

4. CONTROL OF THE SYSTEM

As announced in section 2, to control our system, we use a PQ – control combined with $MPPT$ $P\&O$ control. In this case, system control is shown in Figure 9. PVG is controlled to operate at the maximum by $MPPT$ controller. To simplify, we use a conventional $MPPT$ $P\&O$ [29], [30] in this paper (see Figure 10). The $MPPT$ block delivers a reference current $I_{pv}{}^{*}$ which is used as a reference current by the inverter control (PMI control).

In fact, as shown in Figure 9, a Park transform is carried out with the three-phase current to pass from the abc frame to the Park frame (abc / dq). Two components of current are therefore obtained: d−axis current (I_d) and q−axis current (I_q) which represent the image of active power (P) and reactive power (Q) respectively. Two PI controllers are used to controller these currents (I_d and I_q). These current components are also called direct current (I_d) and quadrature current (I_q).

So by controlling I_d we control active power P indirectly (see equations 32 and 33). And by controlling I_q, reactive power Q is controlled. In this paper, we don't inject reactive power into the grid so as not to disturb it. Hence $I_q = 0$ (see Figure 9), therefore $Q = O$. And I_d current is controlled at the maximum amplitude of the current delivered by $MPPT$ controller. Our system is synchronized with the grid by the phase locked loop (PLL) whose input is a three-phase voltage V_x ($x = a, b, c$) and the output is the rotation angle of the Park transform (θ_e).

Finally, we apply the inverse park transform to obtain three reference voltages. Each reference voltage is compared to a high frequency carrier wave to deliver the PWM signals used to control the MPI inverter, as showing Figure 9.

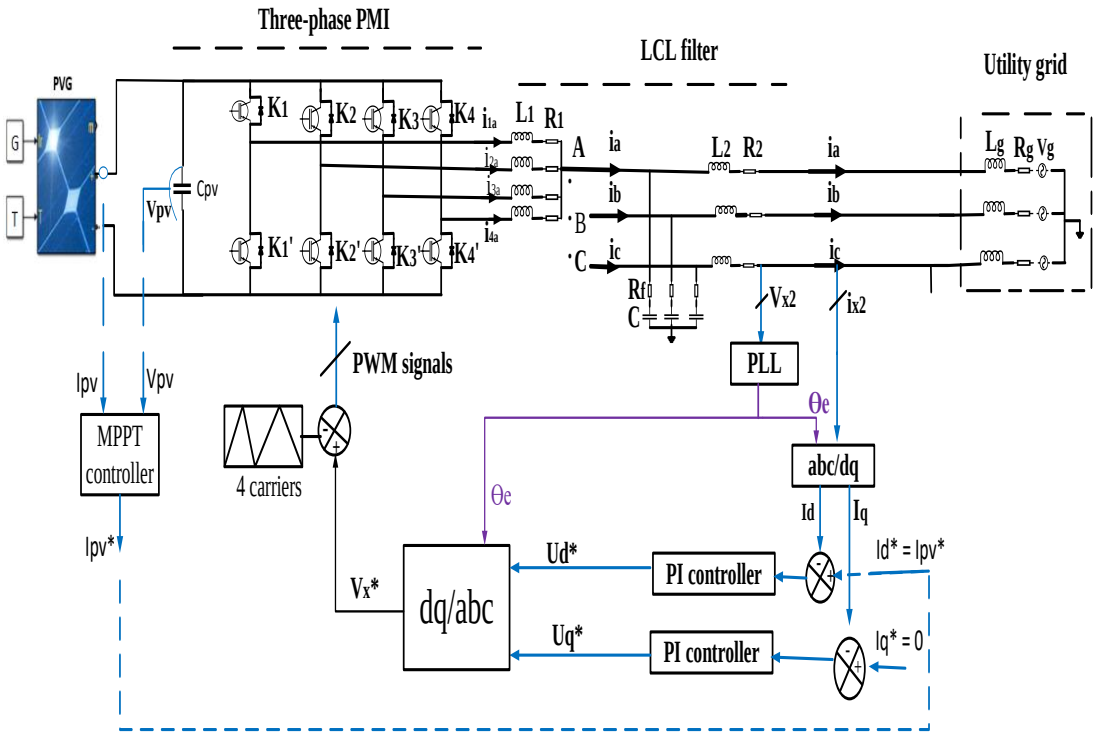

Figure 9. System control

In the next paragraph, we give the principle of the $MPPT$ P&O algorithm based on current perturbation.

4.1. MAXIMUM POWER POINT TRACKING PERTURB AND OBSERVE (MPPT P&O)

The principle of the $MPPT$ $P\&O$ is given in figure 10.

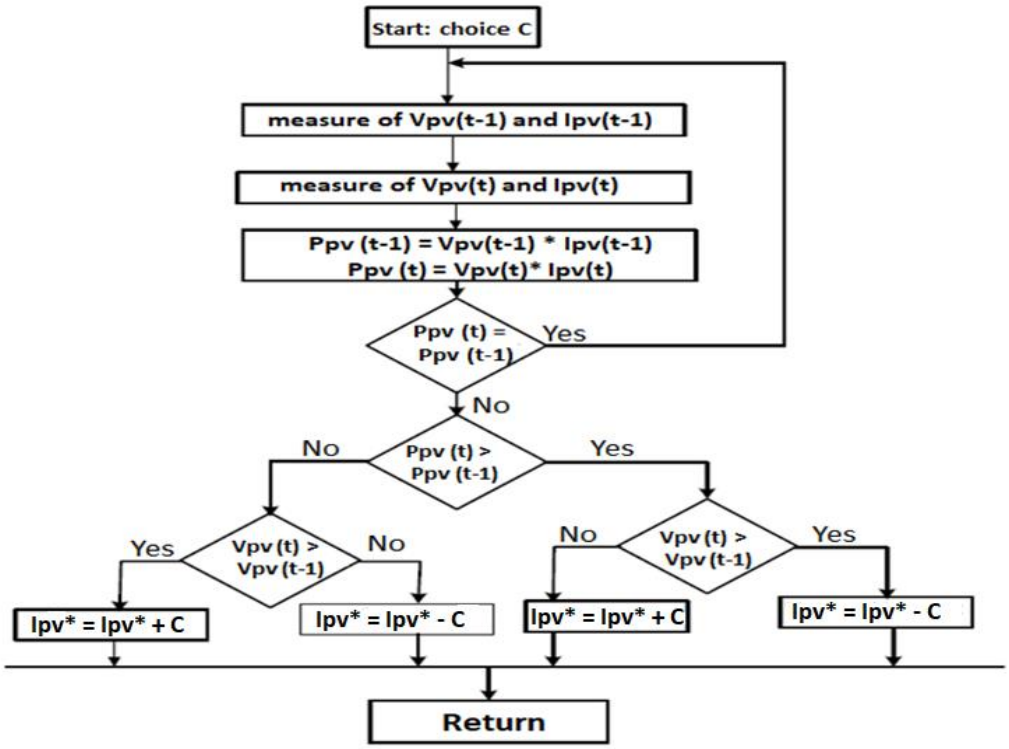

Figure 10. Flowchart of MPPT P&O (based on current)

This *MPPT P&O* algorithm is widely studied in literature, for example in [13], [29] and [30]. Its principle is very simple. We disturb the current (or the voltage) and we see if the power increases or not. In our case, we have chosen to act on the current (with $C = 0.01$) because we need a current at the output of the MPPT block to be used as a reference by the current *PI* controller.

4.2. Powers and Currents Relationship

The active (P) and reactive (Q) powers are written in the Park frame as follows [31]:

$$\begin{cases} P = \frac{3}{2}\left(V_d I_d + V_q I_q\right) \\ Q = \frac{3}{2}\left(V_q I_d - V_d I_q\right) \end{cases} \quad (32)$$

We deduce the components of the dq −axis current in (33).

$$\begin{cases} I_d = \frac{2}{3}\left(\frac{P \cdot V_d + Q \cdot V_q}{{V_d}^2 + {V_q}^2}\right) \\ I_q = \frac{2}{3}\left(\frac{P \cdot V_q - Q \cdot V_d}{{V_d}^2 + {V_q}^2}\right) \end{cases} \quad (33)$$

4.3. Highlighting of the PWM (Pulse Width Modulation)

The principle of the *PWM* is based on comparing fundamental voltage ($V_x{}^*$; $x = a, b, c$) to a carrier high frequency to generate a *PWM* signal used to control an inverter arm. The fundamental frequency signal is equal to the grid frequency ($f = 50$ Hz) whereas the carrier frequency is equal to the switching frequency ($f_{sw} = 20$ kHz). The two switches of the same cell are controlled complementarily (as in the conventional inverter).

Figure 11 shows the details of the *PWM* block for one phase of the inverter. This figure is also valid for the other phases of the inverter but the three references voltages ($V_x{}^*$) are shifted by $2\pi/3$. Each reference voltage is compared with four carriers which they are regularly shifted by $T_{sw}/4$.

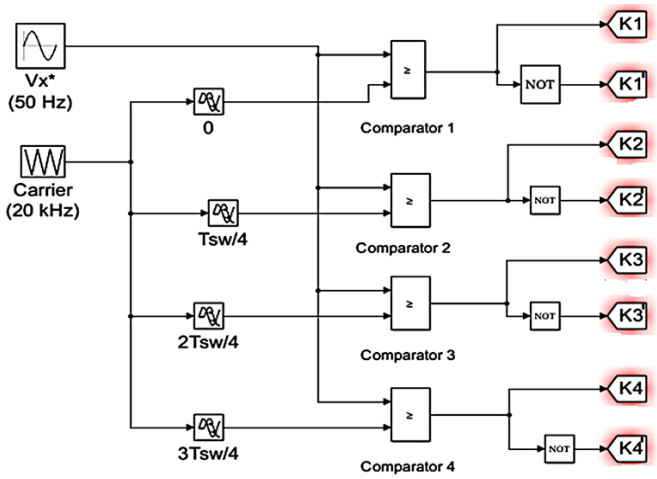

Figure 11. PWM control of one phase of the inverter

4.4. PHASE LOCKED LOOP (PLL)

To synchronize our system on the utility grid. it is necessary to use a PLL. In the literature. several types of PLL are presented but we select the three-phase PLL based voltage also called PLL Park [1], [11] and [16]. Its block diagram is shown in Figure 12. The principle of this PLL is to apply the Park transform to the three-phase grid voltages and adjust the q-axis voltage component (V_q) to zero ($V_q^* = 0$).

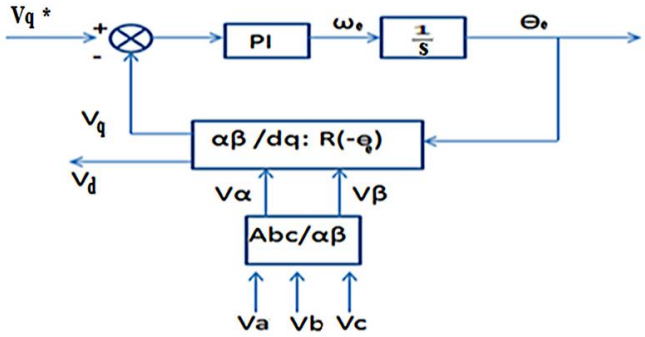

Figure 12. Diagram of the PLL Park **[16]**

Concordia transform is first applied to the grid voltages (V_x) to obtain the alpha-beta voltages ($V_{\alpha\beta}$). Then we do a rotation $R(-\theta_e)$ to obtain dq- voltages (V_{dq}) [16]

Thus. (34) is obtained.

$$\begin{pmatrix} V_d \\ V_q \end{pmatrix} = V\sqrt{3}\begin{pmatrix} \cos(\Theta r - \Theta e) \\ sin(\Theta r - \Theta e) \end{pmatrix} = V\sqrt{3}\begin{pmatrix} \cos(\Delta\Theta) \\ sin(\Delta\Theta) \end{pmatrix} \quad (34)$$

Where $V = 230$ V is the RMS grid voltage. θ_e the estimated angle, and θ_r is the grid voltage angle ($\theta_r = \omega t$).

The PLL locks when $\theta_e = \theta_r$. This condition is achieved if the PI controller regulates V_q to zero.

5. SIMULATION RESULTS AND DISCUSSIONS

5.1. Simulation results

Simulation is done using Matlab Simulink and SimPower Systems by considering the specifications given in Table1 and with the following PI controller parameters:

- PI parameters of the PLL : $k_{p1} = 180$ and $k_{i1} = 3200$
- PI parameters of current (I_d and I_q) controllers: $k_{p2} = 0.05$ and $k_{i2} = 1$
- Sample time: $T_s = 500$ ns

To know how to set the parameters of a PI controller, refer to [16].

In order to test the control, at input of PVG (see Figure 9), we keep temperature constant ($T = 25$ C °) and vary irradiance (G) on time as follows:

- For t ϵ [0 1]s, G $= 1000$ W/m^2,
- For t ϵ [1 2]s, G $= 800$ W/m^2,
- And for t ϵ [2 3]s, G $= 1000$ W/m^2.

Figure 13 shows this irradiance variation on time.

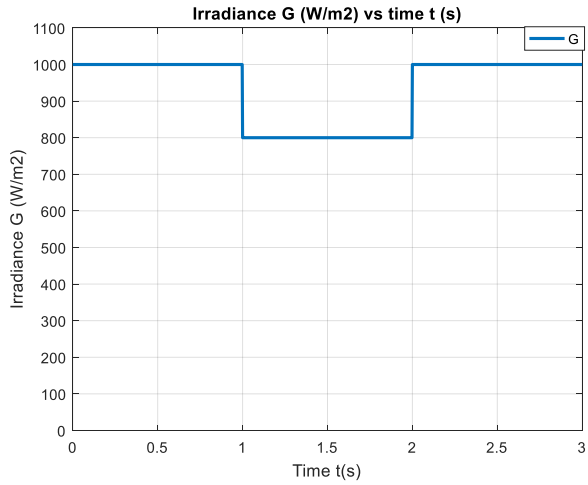

Figure 13. Irradiance (G) variation on time

Somme simulations results are shown in Figure 14 to Figure 21.

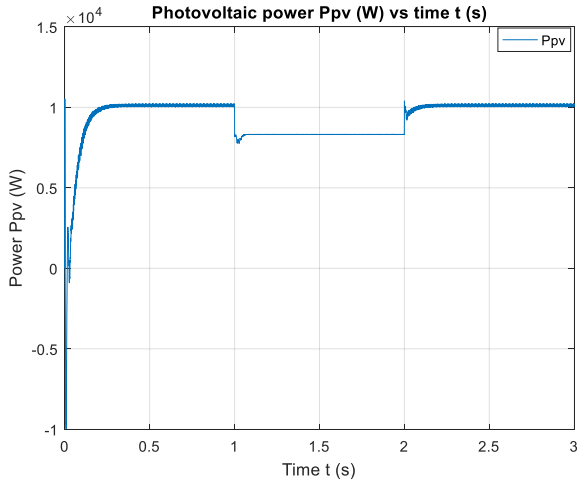

Figure 14. Photovoltaic generator output power ($\boldsymbol{P_{pv}}$) variation

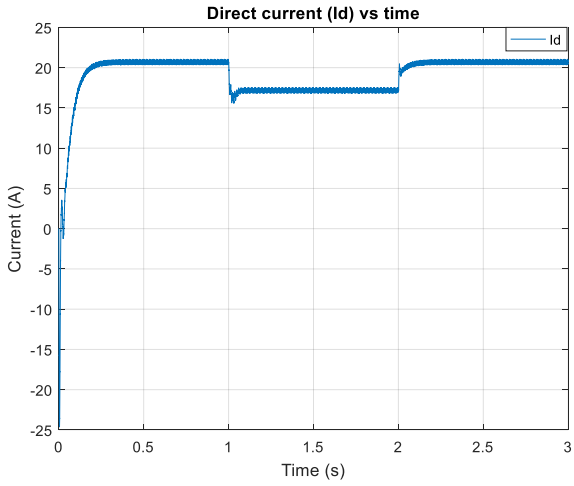

Figure 15. d-axis current ($\boldsymbol{I_d}$) variation

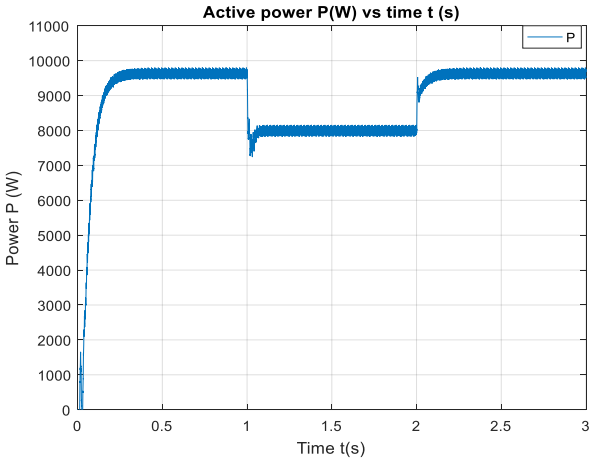

Figure 16. Active power ($\boldsymbol{P}$) variation

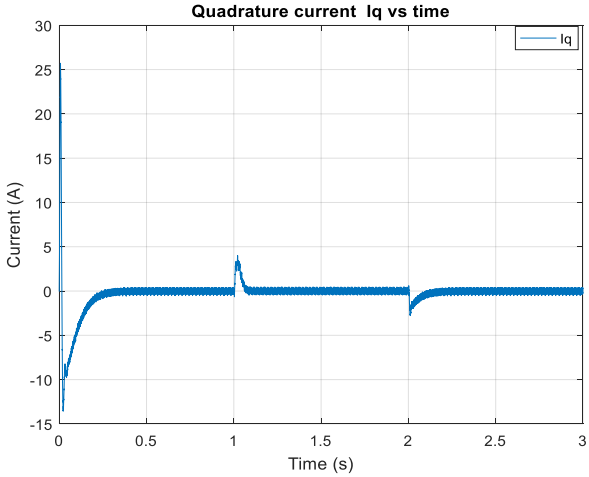

Figure 18. q-axis current ($\boldsymbol{I_q}$) variation

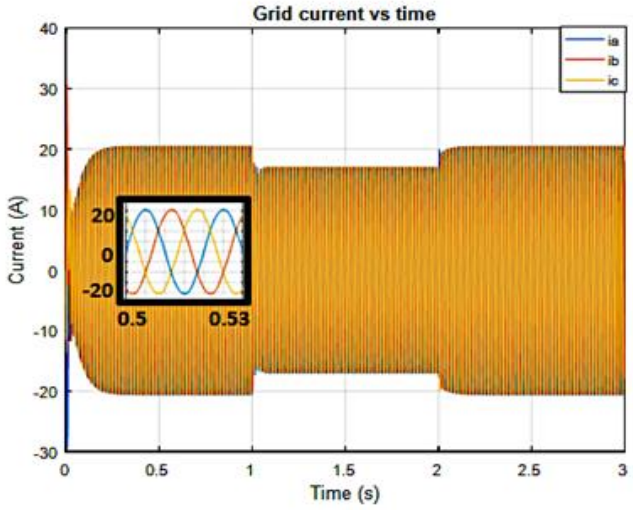

Figure 17. Grid actual current (in the $\boldsymbol{abc}$ frame) variation

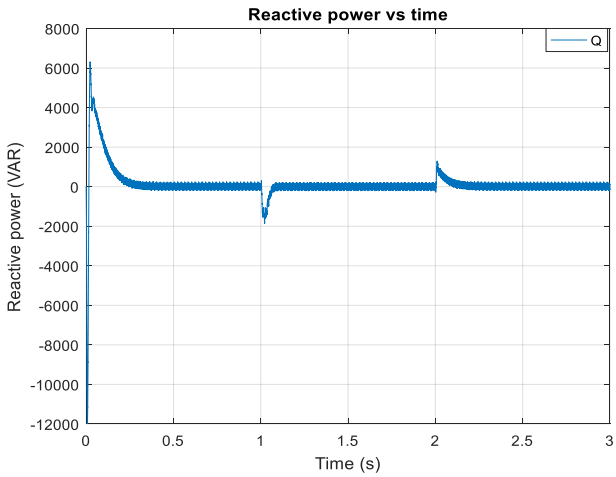

Figure 19. Reactive power ($\boldsymbol{Q}$) variation

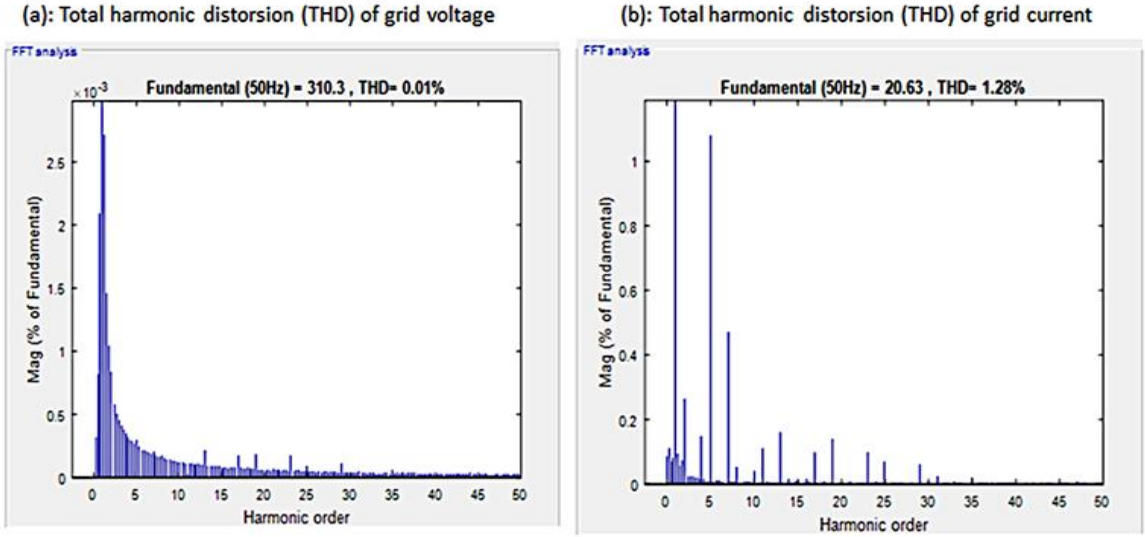

Figure 20. Frequency analysis curves

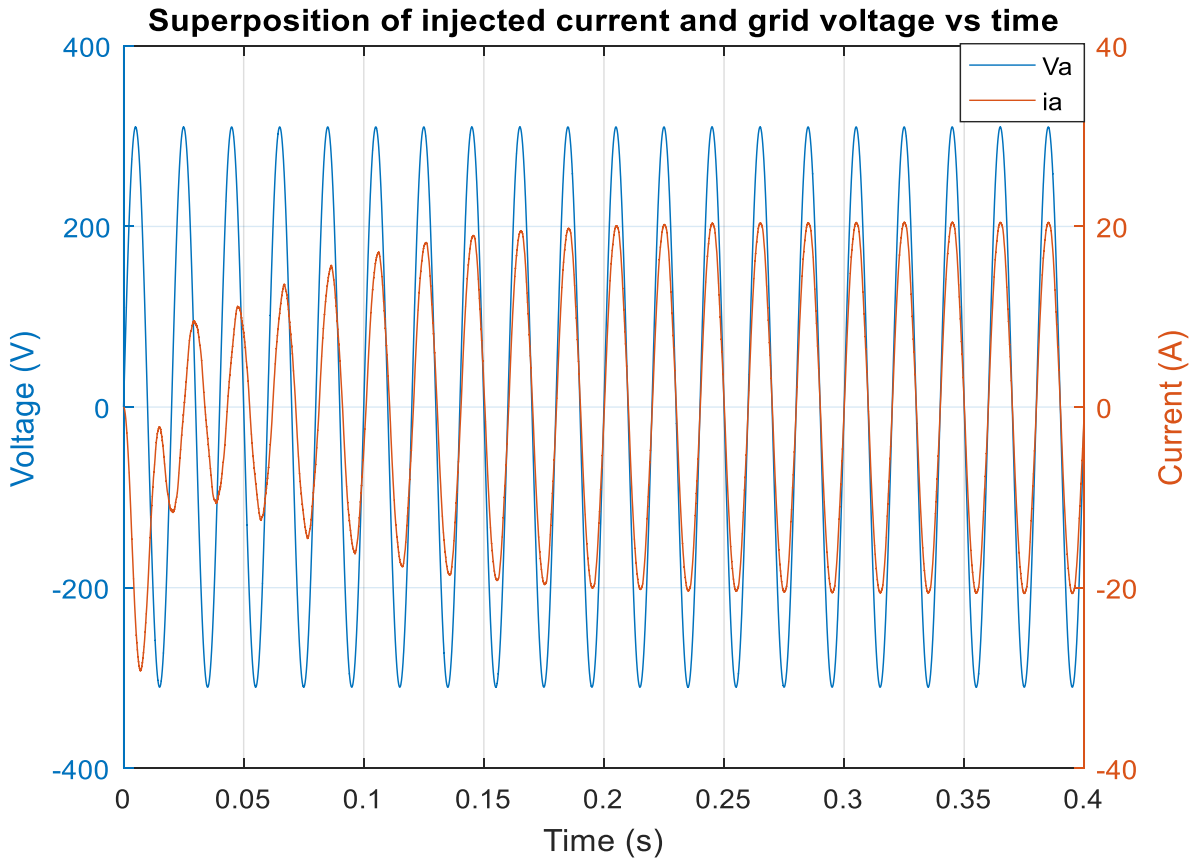

Figure 21. PLL simulation result

5.2. Interpretation of the results

Figure 14 shows the variation of the PVG output power noted P_{pv}. It can be noted that under normal irradiance conditions ($G = 1000\,\mathrm{W/m^2}$), for $t \in [0\ 1]s$ and for $t \in [2\ 3]s$, the power of the PVG is equal to the rated power that we want to inject into the grid ($P_{pv} = P_n = 10$ kW). And for $t \in [1\ 2]s$, irradiance decrease to $G = 800\,\mathrm{W/m^2}$, so $P_{pv} = 8.3$ kW. This effectively corresponds to the power of forty (40) "SolarWord SW260 mono" PV panels under $MPPT$ in the considered conditions of irradiance G.

Figure 15, 16 and 17 show d-axis current ($\mathrm{I_d}$), active power (P) and grid actual current (in the abc frame) variations respectively. They follow the irradiance variation to. That is to say that they increase or decrease according to G. We can see in Figure 16 that, under normal irradiance conditions ($G = 1000\,\mathrm{W/m^2}$), active power is slightly below 10 kW ($P \approx 9.4$ kW). This is normal because it is due to losses. Indeed, the system efficiency is equal to $\eta = 93.6$ %.

The zoom on Figure 17 shows that the actual current (in the abc frame) is quasi-sinusoidal. So LCL filter filtered high frequency harmonics.

Figure 18 and 19 show q-axis current (I_q) and reactive power (Q) respectively. We can see that I_q and Q are always equal to zero in steady state. So we don't inject reactive power Q into the grid. Only active power (P) is injected.

The previous results (from Figure 14 to Figure 19) show that the developed PQ – control combined with MPPT control tracks the references and can be validated.

Figure 20 shows voltage and current total harmonic distortion (THD). We can notice that the THD of voltage is equal to 0.01% (see Figure 20.a) whereas the THD of current is equal to 1.2 % (see Figure 20.b). Both THD respect the $IEE1547$ standard which requires to be smaller than 5 % for the first fifty harmonics [10].

Finally, Figure 21 shows the superposition of one phase (phase a) of injected grid current and grid voltage (of the same phase). We can see that, at the steady state (at $t \approx 100$ ms), the current ($\mathrm{i_a}$) and the grid voltage ($\mathrm{V_a}$) are in phase and have the same frequency ($f = 50$ Hz). So the developed PLL synchronized our system with the grid in about 100 ms.

6. CONCLUSION

The developed PQ-control combined with $MPPT\ P\&O$ control followed the variation of the irradiance (G) by injecting only active power (P) into the grid. Reactive power (Q) is forced to zero. The PLL synchronized our system with the grid in about 100 ms.

The design method made it possible to identify an optimum number of cells at $q = 4$. We have shown in this case that the system efficiency is increased by 7.6 % compared to the conventional system (93.6 % vs 86 %).

The LCL filter has been sized to obtain a THD of voltage equal to 0.01% and a THD of current equal to 1.28 %.

The design method and simulation results showed the value of the PMI. We have shown that the strengths of this inverter is the quality of the waveforms (see Figure 4) and the reliability of the system (several interleaved cells).

However, the disadvantage of the proposed architecture is the number of semiconductors switches used for the PMI fabrication. Fortunately, this disadvantage can be mitigated by the reliability of the system, the system efficiency and the low price of components semiconductors (low class) [20].

REFERENCES

[1] C. Mahamat, Analyse et commandes des convertisseurs multi-niveaux pour un générateurphotovoltaïque connecté au réseau électrique, Thèse de doctorat en génie électrique, Université Paris-Saclay. ffNNT : 2018SACLN024ff. fftel-01824681f, 2018.

[2] M. M. a. B. B. Bouazza Fekkak, Control of transformerless grid-connected PV system using average models of power electronics converters with MATLAB/Simulink, Solar Energy 173 (2018) 804–813, 2018.

[3] M. A. E. M. A. A. G. A. Ahmed Elmelegi, A simplified phase-shift PWM-based feedforward distributed MPPT method for grid-connected cascaded PV inverters, Solar Energy 187 (2019) 1-12, 2019.

[4] F. K. A. R. D. X. Abdeldjabar Benrabah, A New Robust Control for Grid Connected Photovoltaic Systems Based on Active Disturbance Rejection Control, J. Electrical Systems 15-1(2019):81-95, 2019.

[5] S.-H. K. H.-K. L. a. I.-K. W. Ru-Min Chao, Evaluation of a Distributed Photovoltaic System in Grid-Connected and Standalone Applications by Different MPPT Algorithms, Energies. 11. 1484. 10.3390/en11061484, 2018.

[6] M. S. A. A.-D. S. M. M. A. Reznik, LCL Filter Design and Performance Analysis for Grid Interconnected Systems, 2012: Power Electronics and Machines in Wind Application (PEMWA). IEEE . 1-7.

[7] L. H. a. M. K. A.E.W.H. Kahlane, LCL filter design for photovoltaic grid connected systems, Revue des Energies Renouvelables SIENR'14 Ghardaïa (2014) 227 – 232.

[8] A. M. O. a. H. Z. Atiqah Hamizah Mohd Nordin, Modeling and Simulation of Grid Inverter in Grid-Connected Photovoltaic System, INTERNATIONAL JOURNAL OF RENEWABLE ENERGY RESEARCH, Vol. 4, No. 4, 2014., 2014.

[9] S. H. a. F. B. Marco Liserre, Design and control of an LCL-filter based three-phase active rectifier,

Conference Paper in Conference Record - IAS Annual Meeting (IEEE Industry Applications Society) · January 2001.

[10] Standard IEEE1547, IEEE Standard for Interconnecting Distributed Resources with Electric Power Systems, 2003.

[11] J.-P. Gaubert, Générateur photovolatique avec une commande directe de puissance connecté et avec adjonction de services au réseau de distribution., Symposium de Genie Electrique, Jun 2016,Grenoble, France. hal-01361594 . , 2016.

[12] F. K. a. H. M.Makhlouf, Modeling and Simulation of Grid-connected Photovoltaic Distributed Generation System, IEEE conferences, 2012 First International Conference on Renewable Energies and Vehicular Technology,DOI:10.1109/REVET.2012.6195269, 2012.

[13] V.-L. Nguyen, Couplage des systèmes photovoltaiques et des véhicules électriques au réseau : problèmes et solutions., Energie électrique.Université Grenoble Alpes, 2014. Français. <NNT: 2014GRENT056>. <tel-01304703>, 2014.

[14] R. A. A. G. M. Hanan A. Mosalam, Fuzzy logic control for a grid-connected PV array through Z-source-inverter using maximum constant boost control method, Ain Shams Engineering Journal 9 (2018) 2931–2941.

[15] D. M. a. Z. J. ZHENG Fei, Modelling and simulation of Grid-connected PV System inDIgSILENT/PowerFactory, 2nd IET Renewable Power Generation Conference (RPG 2013), DOI:10.1049/cp.2013.1867, 2013.

[16] M. P. R. M. C. G. M. a. F. C. Chabakata MAHAMAT, Decoupled PQ control Applied to a Multicellular Parallel Inverter for Grid-connected Photovoltaic System, IEEE conferences publications, 2016 17th International Conference on Sciences and Techniques of Automatic Control and Computer Engineering (STA), DOI10.1109/STA.2016.7952002, 2016.

[17] S. World, Sunmodule plus SW260 -270 mono, https://www.axun-solar.com/docs/panneau/solarworld/AXUN_FICHE_TECHNIQUE_SUNMODULE_PLUS_mono_260-270_fr.pdf.

[18] S. B. a. R. Saini, A mathematical modeling framework to evaluate the performance of single diode and double diode based SPV systems, Energy Reports 2 (2016) 171–187.

[19] S. S. a. M. F. N. Tanvir Ahmad, Comparative Analysis between Single Diode and Double Diode Model of PV Cell: Concentrate Different Parameters Effect on Its Efficiency, Journal of Power and Energy Engineering, 2016, 4, 31-46.

[20] M. P. F. C. R. M. a. A. M. Chabakata Mahamat, Balanced Active and Reactive Control Applied to a Grid Connected Five Level Inverter, (IJACSA) International Journal of Advanced Computer Science and Applications,Vol. 8, No. 10, 2017, 2017.

[21] F. ADAM, Onduleur multicellulaire parallèle à ICT : commande équilibrante analyse, modélisation et optimisation des performances CEM, Thèse de doctorant en ELECTRONIQUE – ELECTROTECHNIQUE-AUTOMATIQUE, ENS-CACHAN, 2011.

[22] K. GUEPRATTE, Onduleur triphasé à structure innovante pour application aéronautique, These de dotorat en génie électrique, Université de Grenoble, 2011.

[23] T. M. G. a. Y. X. Hongfei Wu, Full-Range Soft-Switching Isolated Buck-Boost Converters With Integrated Interleaved Boost Converter and Phase-Shifted Control,

DOI10.1109/TPEL.2015.2425956, IEEE Transactions on Power Electronics, 2016.

[24] B. Huang, Convertisseur continu-continu à rapport de transformation élevé pour applications pile à combustible, Institut National Polytechnique de Lorraine, 2009. Français. ffNNT :2009INPL021Nff. fftel-01748756f, 2009.

[25] M. P. F. C. R. M. A. M. Chabakata Mahamat, Optimized Design of an LCL Filter for Grid Connected Photovoltaic System and Analysis of the Impact of Neighbors' Consumption on the System., Journal of Electrical Systems, ESR Groups. ⟨hal-01676019⟩, 2017.

[26] F. F. Jean-Paul Ferrieux, Alimentations à découpage Convertisseurs à résonance, Principes composants-modélisation, CACHAN: Bibliothèque de l'ENS-CACHAN: 3e edition DUNOD,Paris, 1999.

[27] EPCOS, Ferrites and Accessories, EPCOS DATA Book 2013: https://www.tdk-electronics.tdk.com/download/519704/069c210d0363d7b4682d9ff22c2ba503/ferrites-and-accessories-db-130501.pdf.

[28] INFINEON, TechnischeInformation/TechnicalInformation: module FS10R12VT3, https://www.infineon.com/cms/en/product/power/igbt/igbt-modules/fs10r12vt3/.

[29] N. Z. Y. N. S. a. M. W. U. Oladimeji Ibrahim, Matlab/Simulink Model of Solar PV Array with Perturb and Observe MPPT for Maximising PV Array Efficiency, Johor Bahru, Malaysia: 2015 IEEE Conference on Energy Conversion (CENCON),DOI: 10.1109/CENCON.2015.7409549.

[30] T. D. a. R. K. Tekeshwar Prasad Sahu, Simulation and Analysis of Perturb and Observe MPPT Algorithm for PV Array Using ĊUK Converter, Advance in Electronic and Electric Engineering.ISSN 2231-1297, Volume 4, Number 2 (2014), pp. 213-224.

[31] B. A. L. H. E. S. a. J.-S. L. Huibin Zhu, Grid Synchronization Control without AC Voltage Sensors, Miami Beach, FL, USA, USA: IEEE conferences publications, DOI: 10.1109 / APEC.2003.1179210, 2003.

[32] C.-S. L.-C. W. a. Y.-D. H. Wai-Hei Choi, Analysis of DC-Link Voltage Controls in Three-Phase Four-Wire Hybrid Active Power Filters, IEEE TRANSACTIONS ON POWER ELECTRONICS, VOL. 28, NO. 5, MAY 2013, 2013.

[33] P. O. L. D. B. C. M. F. K. &. A. N. A. Charki, Lifetime assessment of a photovoltaic system using stochastic Petri nets, International Journal of Modelling and Simulation, 2017.

[34] T. K. H. B. A. B. M. S. H. A Darkawi, Modélisation, Commande et Mise en Oeuvre de deux Ponts Triphasés Back-to-Back avec Contrôle des Flux de Puissance et de la Tension du Bus DC : Application à l'émulation de la chaîne de conversion électrique des houlogénérateurs directs., La Revue 3 E. I, Société de l'électricité, de l'électronique et des technologies de l'information et de la communication, 2015, pp.61-71. <hal-01208538>, 2015.

[35] M. P. F. C. R. M. A. M. Chabakata Mahamat, Optimized Design of an LCL Filter for Grid Connected Photovoltaic System and Analysis of the Impact of Neighbors' Consumption on the System, J.Electrical Systems 13-4(2017):618-632, 2017.